Analytical prediction of the seismic behaviour of superelastic shape memory alloy reinforced concrete elements

M.S. Alam, M.A. Youssef, M. Nehdi *

Department of Civil and Environmental Engineering, The University of Western Ontario, London, Ontario, Canada, N6A 5B9

ABSTRACT

Superelastic shape memory alloys (SMAs) are unique materials that have the ability to undergo large deformations, but can return to their undeformed shape by the removal of stress. If such materials can be used as reinforcement in plastic hinge regions of beam–column elements, they will not only experience large inelastic deformations during strong earthquakes, but can potentially recover their original shape. This behaviour will allow mitigating the problem of permanent deformation. Hence, this study aims at establishing guidelines for predicting the seismic behaviour of concrete beam–column elements reinforced with superelastic SMAs. The paper identifies the disparities in moment–curvature relationship between SMA and steel reinforced sections. Then it examines the applicability of existing methods developed for steel reinforced concrete (RC) members to predict the length of the plastic hinge, crack width, crack spacing, and bond-slip relationship for superelastic SMA RC elements. Existing superelastic SMA models are discussed and the application of one of the models in a finite element (FE) program is presented. This FE program is used to simulate the behaviour of an SMA RC column and a beam–column joint. The predicted load–displacement, moment–rotation relationships and energy dissipation capacities have been found to be in good agreement with experimental results.

© 2008 Elsevier Ltd. All rights reserved.

1. Introduction

Buildings and bridges in high seismic regions are prone to severe damage and collapse during earthquakes due to large lateral deformations. In particular, beam–column elements in reinforced concrete (RC) structures are extremely vulnerable and are considered the weakest link in such a structural system [1]. Current seismic design codes emphasize earthquake resistant structures to be sufficiently ductile by proper reinforcement detailing at critical regions in order to ensure elastic behaviour under moderate earthquakes. However, it is difficult and costly to build structures that can perform elastically under strong ground motion. In conventional seismic design of RC structures, reinforcing bars are expected to yield in order to dissipate energy while undergoing permanent deformations of post-yield steel reinforcing bars and damage of unconfined concrete. Consequently, during large-scale earthquake events, severe damage of infrastructure occurs resulting in the collapse of buildings, closing of bridges, unattainable post-disaster rescue operations, and overall substantial economic losses. These can generally be avoided if structures were serviceable after such earthquakes.

Superelastic (SE) SMA is a special material that can undergo large inelastic deformations and recover its original shape by stress removal, thus mitigating the problem of permanent deformation. Because of its unique characteristics, SMAs have gained increased usage in structural applications [2] for instance, as column anchorage [3], frame bracing [4], concrete prestressing [5], damping device [6,7], and bridge restrainers [8]. Ocel et al. [9] used SMAs in steel beam–column connections, which displayed repeatable and stable hysteretic behavior. Auricchio et al. [10] and Zhu and Zhang [11] conducted numerical simulations and compared the seismic responses of steel frame buildings equipped with traditional steel bracings and SE SMA bracings. Their results showed that buildings with SMA bracings performed better than steel braced buildings in terms of inter-storey and residual drift. Krstulovic-Opara et al. [12] performed a numerical investigation on the use of high-performance concrete reinforced with SMA fibres and its effect on the structural response of a SMA-HPFRC frame structure. Saiidi et al. [13] investigated the effectiveness of SE SMA RC beams in reducing permanent deformation where SMA was used as tensile reinforcement only at the critical region of the beam. Recent tests conducted by Saiidi and Wang [14] and Youssef et al. [15] showed that SE SMA RC elements are capable of dissipating significant amounts of energy with negligible residual deformation and rotation during earthquakes. This extraordinary characteristic of SE SMA-RC beam–column elements can be of great benefit in high seismic areas as RC members will remain functional even after a strong earthquake. SMAs' high strength, large energy hysteretic behaviour, full recovery of strains up to

List of Notations

f_y	Yield stress of rebar; SMA's yield is being used to refer to the initiation of phase transformation, i.e. Austenite to martensite starting stress of SMA (Fig. 1(b))
f_{P1}	Maximum stress of SMA up to its superelastic strain range (Fig. 1(b))
f_{T1}	First stage of unloading stress of SMA (Fig. 1(b))
f_{T2}	Second stage of unloading stress of SMA (Fig. 1(b))
ε_l	Superelastic plateau strain length of SMA (Fig. 1(b))
E_s	Modulus of elasticity of SMA in martensite state
E_a	Modulus of elasticity of SMA in austenite state
α	The ratio of f_y under tension and compression
A_f	Austenite finish temperature
θ_e	Elastic rotation
θ_p	Plastic rotation
L	Length of the member
L_p	Plastic hinge length
ϕ_y	Curvature at which rebar yields
ϕ_u	Maximum curvature in the inelastic range
Δ_y	Displacement at which rebar yields
Δ_u	Maximum displacement in the inelastic range
d	Effective depth of the member
d_b	Bar diameter
ε_s	Strain in the rebar
C	Concrete clear cover
S	Maximum spacing between longitudinal rebars
S_{ave}	Average spacing between longitudinal rebars
A_{ceff}	Effective tensile area of concrete surrounding the tension rebars and having the same centroid as that of the rebars
A_{s1}	Area of each rebar
f_c'	Concrete compressive strength
w_m	Mean crack width
w_{max}	Maximum crack width
S_m	Crack spacing
h_1	Distance from the centroid of the tension rebar to the neutral axis
h_2	Distance from the extreme tension fiber to the neutral axis
n	Number of rebar in the tension zone
ε_1	Maximum tensile strain in the effective zone
ε_2	Minimum tensile strain in the effective zone
A_s	Area of rebar in the tensile zone
f_s	Stress in the reinforcement at specified loads calculated using elastic cracked section theory
d_c	Distance from the extreme tension fiber to the center of the rebar located closest to it
k	A coefficient which is equal to 11×10^{-6} for conventional RC members, found as $40.9 \times 10^{-6} \pm 9.5 \times 10^{-6}$ for FRP RC members
ρ	Reinforcement ratio
E_s	Modulus of elasticity of rebar
k_1	A coefficient having a value of 1.6 for plain bars and 0.8 for deformed bars
k_2	A coefficient having a value of 0.5 for members subjected to bending and 1.0 for members subjected to tension
s_{st}	Axial elongation of steel
s_{SMA}	Axial elongation of SMA
s_e	Extensometer reading from the pullout test
s	Bar slip at the joint
T	Bar force from the pullout test
P	Force applied at the beam tip of the beam–column joint
h	Beam depth
d'	Distance from the centre of the top bar to the top beam face

8%, high resistance to corrosion and fatigue make them strong contenders for use in earthquake resistant structures [16]. In particular, Ni–Ti alloy has been found to be the most promising SMA for seismic applications.

This paper examines the fundamental characteristics of SE SMA and its modelling technique. It also aims at defining methods to predict the behaviour of superelastic SMA RC beam–column elements in terms of its moment–curvature relationship, plastic hinge length, crack width, crack spacing, and bond-slip relationship. Nonlinear FE analysis has been implemented in this study to predict the load–displacement relationship and energy dissipation capacity of superelastic SMA RC beam–column elements. These predictions are compared with experimental results.

2. Research significance

The seismic design of structures has evolved towards a performance-based approach in which there is need for new structural members and systems that possess enhanced deformation capacity and ductility, higher damage tolerance, decreased residual crack size, and recovered or reduced permanent deformations. The use of superelastic SMA as reinforcement instead of steel in the hinge locations of beams and columns has not only proved to dissipate adequate seismic energy, but could also restore the original shape of such members after seismic actions. Such SMA reinforced beam–column elements could allow structural engineers to design RC connections exhibiting little damage and mitigating post earthquake joint repairs. SMA has a relatively lower modulus of elasticity and smaller hysteretic loop compared to that of steel. Therefore, using SMA as reinforcement in RC sections may result in significant changes in the behaviour of RC structures, thus having practical importance in their design. This paper discusses critical and essential design features of SMA RC structures from the analytical point of view. It provides numerical tools and guidelines that should prove to be essential for designers in the near future.

3. Superelastic shape memory alloys

Superelasticity is a distinct property that makes SMA a smart material. A SE SMA can restore its initial shape spontaneously even from its inelastic range upon unloading. Among various composites, Ni–Ti has been found to be the most appropriate SMA for structural applications because of its large recoverable strain, superelasticity and exceptionally good resistance to corrosion. In this paper, unless otherwise stated, SMAs are mainly referred to Ni–Ti SMA (commonly known as Nitinol).

A SMA exhibits superelasticity as long as it is in the austenite state. When an austenite SMA is loaded and unloaded, six distinctive characteristics can be recognized in the stress strain diagram (Fig. 1(a)): (a) elastic response of austenite at low strains ($<1\%$) as denoted by BC, (b) stress-induced transformation from austenite to martensite with a long and constant stress plateau at intermediate and large strains as indicated by CD, (c) elastic response in the stress-induced martensite state at large strains represented by DE, (d) elastic recovery of strain upon stress removal as shown by EF, (e) instinctive recovery of strain at almost a constant stress path because of the reverse transformation to austenite due to the instability of martensite as depicted by FG, and finally (f) elastic recovery in the austenite phase as indicated by GB [16]. This exceptional ability of SMA to recover substantial inelastic deformation upon unloading yields a characteristic hysteresis loop, which is known as superelasticity. SMA with superelasticity has an advantage over other common metals/alloys in the sense that besides dissipating a considerable amount of energy under repeated load cycles, it has a negligible residual strain.
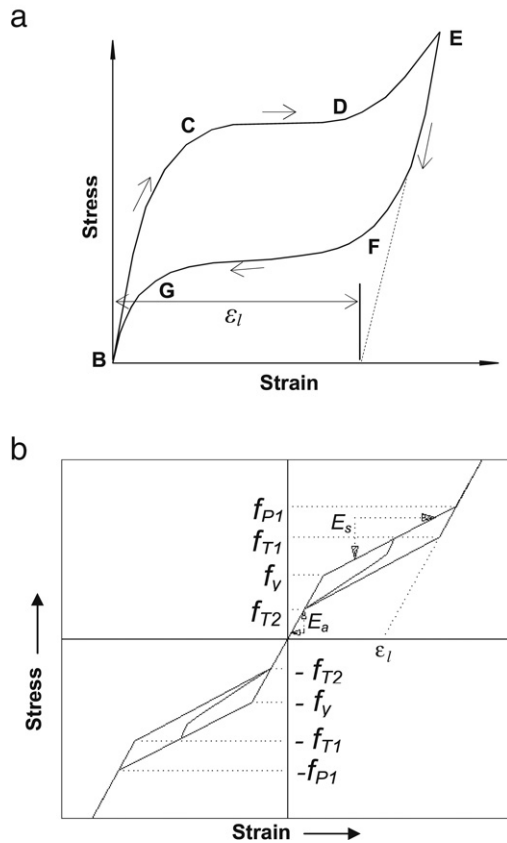
a

b

Fig. 1. (a) Typical axial stress–strain diagram of superelastic SMA, (b) 1D-superelastic model of SMA incorporated in FE Pacakges (reprinted from Auricchio et al. [24] with permission).

3.1. Modeling SMA

Since most civil engineering applications of SMA are related to the use of bars and wires, one-dimensional phenomenological models are often considered suitable. Several researchers have proposed uniaxial phenomenological models for SMA [17–20]. The superelastic behavior of SMA has been incorporated in a number of finite element packages, e.g. ANSYS 10.0 [21], ABAQUS 6.4 [22] and Seismostruct 4.0.2 [23] where the material models have been defined using the models of Auricchio et al. [24], Auricchio and Taylor [25], and Auricchio and Sacco [26], respectively. Fig. 1(b) shows the 1D-superelastic model used in ANSYS 10.0 [21] where SMA has been subjected to multiple stress cycles at a constant temperature and undergoes stress induced austenite-martensite transformation. The parameters used to define the material model (Fig. 1) are yield stress, f_y (point C); maximum stress up to the superelastic strain range, f_{P1} (point E); first stage of unloading stress, f_{T1} (point F); second stage of unloading stress, f_{T2} (point G); superelastic plateau strain length, ε_l; moduli of elasticity, E_s

and E_a; and the ratio of f_y under tension and compression, α. Although a SMA does not have a yielding process, yield is being used to refer to the initiation of phase transformation of SMA. Fig. 2 shows stress–strain curves of the SMA model [24] with a complete transformation path followed by (a) cycles with partial loading (PL) and partial unloading (PU), (b) cycles with PL and complete unloading (CU), and (c) cycles with complete loading (CL) and PU, respectively. Here, PL and PU refer to incomplete stress induced phase transformation, whereas CL and CU refer to complete stress induced transformation in the loading-unloading process. Fig. 2 highlights the stress–strain behavior of SE SMA under cyclic axial loading of varying amplitudes.

4. Experimental study on SMA RC elements

This section briefly describes the available experimental studies conducted on SMA RC beam–column elements under seismic loading.

4.1. SMA RC beam–column joint

Two large-scale beam–column joints were tested under reversed cyclic loading by Youssef et al. [15]. The first joint was reinforced with regular steel rebars, while the other was reinforced with SMA at the plastic hinge region of the beam, along with regular steel in the remaining portion of the joint (specimen JBC-2). Hot-rolled Ni–Ti alloy (55.0% nickel and 45.0% titanium by weight) rebar was used as reinforcement in the JBC-2 specimen. Its austenite finish temperature, A_f, defining the complete transformation from martensite to austenite, ranges from −15 to −10 °C. Both joints were designed according to Canadian standards [27]. The detailed design of joints JBC-1 and JBC-2 is given in Fig. 3(a). In the case of JBC-2, single barrel screw lock couplers [28] were used for connecting steel and SMA rebars. The couplers used are mechanical connectors consisting of smooth shaped steel sleeves with converging sides. Each end of the reinforcing bars is inserted into one of the coupler ends until it reaches the middle pin (center stop). Both rebars meet head to head separated by a pin at the middle. Screws with smooth ends are used to hold the rebars, which are tightened until their heads are sheared off indicating that the required torque is reached. Fig. 3(b) and (c) illustrate the splice details and couplers used in the reinforcement caging of JBC-2, respectively. The material properties for both specimens are presented in Table 1. Some experimental results of both specimens in terms of yield and ultimate values of curvatures and beam-tip displacements, plastic hinges, crack width and crack spacing are presented in Tables 2 and 3.

4.2. SMA RC column

Two quarter-scale spiral RC columns representing RC bridge piers were designed, constructed and tested using a shake table by Saiidi and Wang [14]. Fig. 4 shows the reinforcement detailing of the bridge pier (specimen SMAC-1) where SMA rebars are placed
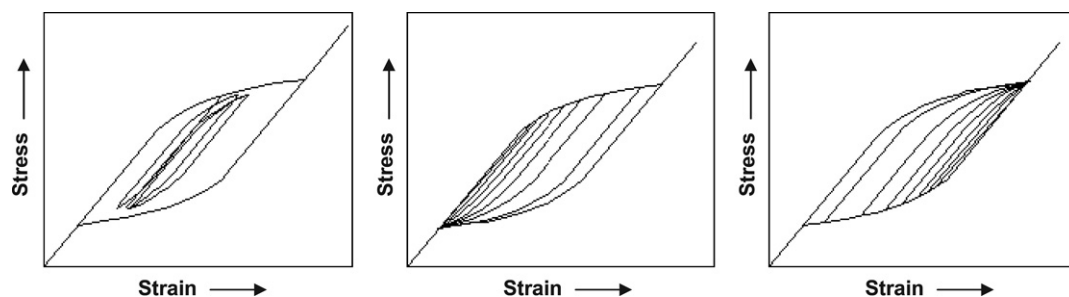

Fig. 2. 1D-Superelastic model of SMA at constant temperature where the stress–strain curves are drawn after a complete transformation path followed by (a) PL and PU, (b) PL and CU, and (c) CL and PU (reprinted from Auricchio et al. [24] with permission).
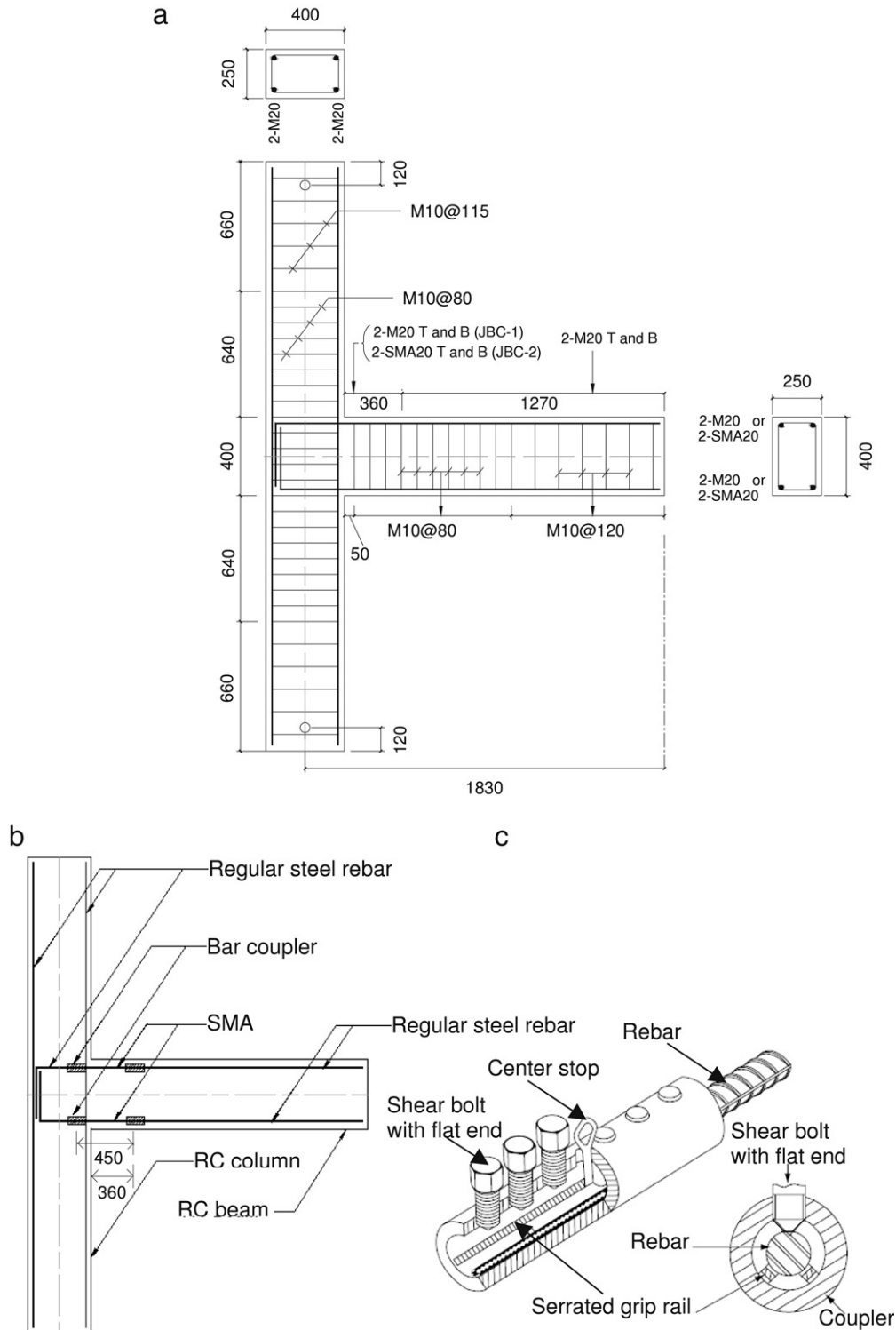
Fig. 3. (a) Reinforcement details of specimens JBC-1 and JBC-2, (b) Splice details of specimen JBC-2, (c) single barrel screw-lock coupler for connecting SMA rebar with regular steel rebar (all dimensions in mm).

at the plastic hinge region and connected to the steel rebars with threaded mechanical couplers. Ni–Ti alloy (55.9% nickel and 44.1% titanium by weight) with austenite finish temperature, A_f of approximately 0 °C was used as reinforcement. The mechanical properties of the materials used are presented in Table 1. The yield and ultimate values of curvature and top-displacement, and the length of the plastic hinge of the column are presented in Table 2. Saiidi and Wang [14] observed that SMA-RC columns were superior

to conventional steel-RC columns in limiting relative column top displacement and overall residual displacements; they withstood larger earthquake amplitudes compared to that for conventional columns.

5. Analytical prediction

This section deals with the analytical prediction of moment–curvature, plastic hinge length, crack width and crack spacing of

Table 1
Material properties for specimens JBC-1, JBC-2 and SMAC-1

Material	Property	JBC-1	JBC-2	SMAC-1
Concrete	Compressive strength (MPa)	53.5	53.7	43.8
	Strain at peak stress (%)	0.2	0.2	0.2
	Tensile strength (MPa)	3.5	2.8	4.0
Longitudinal steel (JBC-1 & 2: Ø19.5 mm, SMAC-1: Ø15.9 mm)	Yield strength (MPa)	520	450	439
	Ultimate strength (MPa)	630	650	708
	Young's modulus (GPa)	198	193	200
Transverse steel (JBC-1 & 2: Ø11.3 mm, SMAC-1: Ø4.9 mm)	Yield strength (MPa)	422	422	469
	Ultimate strength (MPa)	682	682	540
SE SMA (JBC-1 & 2: Ø20.6 mm, SMAC-1: Ø12.7 mm)	Modulus of elasticity, E_{SMA} (GPa)	–	62.5	39.7
	f_y as in Fig. 1(b) (MPa)	–	401	379
	f_{P1} as in Fig. 1(b) (MPa)	–	510	405
	f_{T1} as in Fig. 1(b) (MPa)	–	370	180
	f_{T2} as in Fig. 1(b) (MPa)	–	130	100
	ε_l as in Fig. 1(b) (%)	–	6.00	5.5

Table 2
Calculation of plastic hinge lengths using different methods

Specimen	Cross-sectional area (mm²)	d_b (mm)	L (mm)	f_y (MPa)	f_c' (MPa)	Experimental					Analytical			Empirical			
						Δ_y (mm)	Δ_u (mm)	ϕ_y (rad/km)	ϕ_u (rad/km)	L_p (Eq. (7)) (mm)	ϕ_y (rad/km)	ϕ_u (rad/km)	L_p (Eq. (5)) (mm)	L_p (Eq. (8)) (mm)	L_p (Eq. (9)) (mm)	L_p (Eq. (10)) (mm)	L_p (Eq. (11)) (mm)
Steel RC BCJ, JBC-1	100 000	19.5	1630	520	53.5	12	72	8.3	117	384	7.5	76.4	156	222	282	281	353
SMA RC BCJ, JBC-2	100 000	20.6	1630	401	53.7	18	72	22	122	374	18.0	91.3	131	222	282	281	312
SMA RC Column, SMAC-1 (Wang 2004)	72 966	12.7	1372	379	40.3	11	66	17	210	228	22.1	242.8	172	179	232	221	216

Table 3
Predicted maximum crack width and average crack spacing of specimen JBC-1 and JBC-2

Reference	Equation No.		Steel RC BCJ, JBC-1		SMA RC BCJ, JBC-2	
	w_{max} (mm)	S_m (mm)	w_{max} (mm)	S_m (mm)	w_{max} (mm)	S_m (mm)
Experimental	–	–	2.6	113.3	10.7	197.5
Oh and Kang [34]	Eq. (12)	Eq. (13)	5.1	130.7	6.7	133.3
CEB-FIP Code [35]	Eq. (16)	Eq. (14)	6.6	147.3	8.5	204.8
Chowdhury and Loo [39]	Eq. (20)	Eq. (18)	5.5	235.6	6.6	221.1
Eurocode 2 [40]	1.7 × Eq. (22)	Eq. (21)	2.9	141.1	10.0	223.1
Gergely–Lutz [37]	Eq. (17)	–	0.48	–	0.46	–
Masmoudi et al. [38]	Eq. (17)	–	1.8	–	1.7	–

steel and SMA-RC beam–column elements and compares findings with the experimental results. The bond-slip relationship and joint shear have also been discussed.

5.1. Moment–curvature relationship

The flexural behaviour of a RC section largely depends on the relationship between moment, curvature, and axial force. The moment (M)–curvature (φ) relationship depends on the material properties, geometry and arrangement of rebars in the cross-section of a RC member.

It is important to make proper assumptions for stress (σ)–strain (ε) curves of the materials for accurate prediction of the M–φ relationship. Scott et al. [29] model has been used for the σ–ε relationship of confined concrete, while the bilinear kinematic strain hardening model has been used for steel and SMA σ–ε curves with strain hardening parameters of 0.020 and 0.037, respectively. At large strains, unconfined concrete, outside the stirrups will spall off and will not contribute to the capacity of the member. Since this spalling is usually a gradual process, it is difficult to determine a particular strain at which spalling commences. It is assumed that the cover concrete follows the σ–ε curve of unconfined concrete according to the Scott et al. [29] model up to a strain of 0.004, but carries no stresses at

higher strains. An incremental deformation technique has been used to determine the moment and its corresponding curvature at a particular strain distribution.

Fig. 5 shows the theoretical M–φ diagrams for the beams of JBC-1, JBC-2 and SMAC-1. The cracking moment of JBC-1 was 22.7 kN m at a curvature of 0.42 rad/km, whereas JBC-2 experienced cracking at a moment of 19.1 kN m at a curvature of 0.43 rad/km. The yield moments were reached at curvatures of 7.5 rad/km and 18.0 rad/km for JBC-1 and JBC-2, respectively. However, the moment capacities of JBC-1 and JBC-2 were found to be almost equal. The energy dissipation capacities of JBC-1 and JBC-2 under static loading were calculated as 1.1 kN m and 0.87 kN m, respectively using M–φ diagrams. It was observed that specimen JBC-2 and SMAC-1 suffered a significant amount of curvature before yielding of SMA compared to that of JBC-1. This is mainly due to the lower stiffness of SMA rebar compared to that of steel. SMAC-1 showed larger ductility compared to JBC-1 and JBC-2, which is mainly due to higher confinement by spiral reinforcements.

5.2. Plastic hinge length

The plastic hinge length of a structural member is an essential parameter in evaluating the response of a structure and its damage
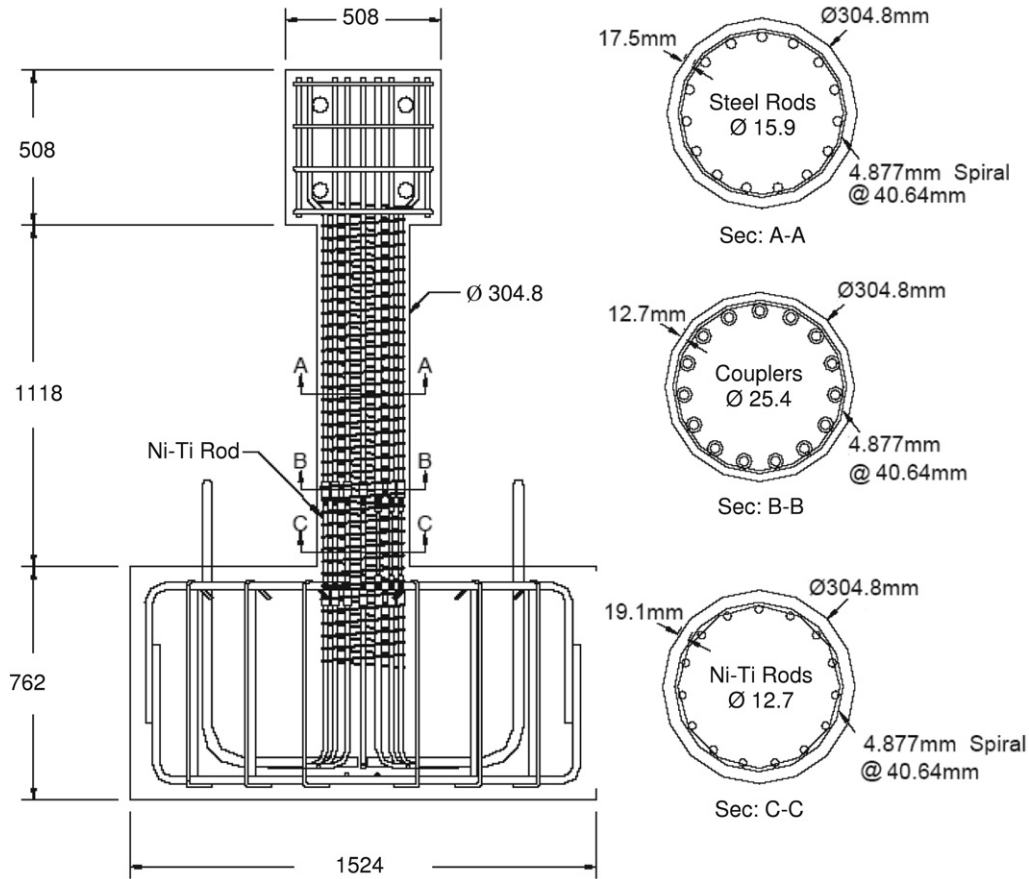
Fig. 4. Reinforcement details of SMA RC Column (Saiidi and Wang [14], with permission).
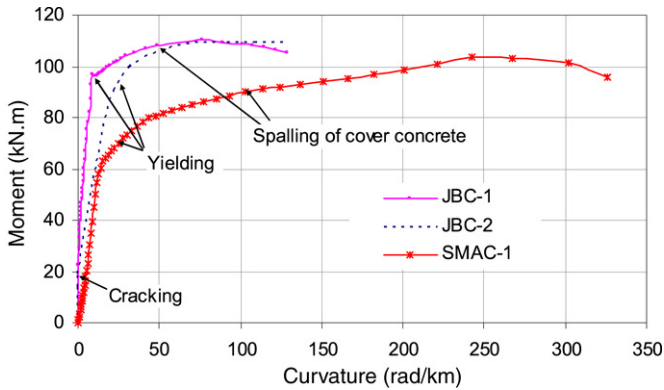

Fig. 5. Moment–curvature relationship of JBC-1, JBC-2, and SMAC-1.

due to seismic and/or other loads. Numerous techniques and models are available to estimate the plastic hinge length of RC members as described below.

5.2.1. Analytical method

From the moment–curvature relationship of a RC section, the ultimate moment can be chosen. Its corresponding load is calculated and applied at the beam/column tip. Subsequently, the curvature is distributed along the member length with respect to its moment ordinates. The curvature distribution along the length of the member (L) is constructed for specimens JBC-1, JBC-2 and SMAC-1 (Fig. 6) in order to determine their plastic hinge rotation and length. The rotation of the beam from the beam tip and column face, θ can be calculated by summing the curvature over its entire length, which is the summation of elastic rotation

(θ_e) and plastic rotation (θ_p) (Eq. (1)). The curvature distribution is then idealized with distinct yield and ultimate curvature values. To create this model, a line, OE is extended from the origin parallel to the initial part of the curvature-distance graph as shown in Fig. 6. A perpendicular line, AB is drawn from the point of maximum curvature ordinate, A to the distance axis where AB intersects OE at E. Here, E and A represent the yield and ultimate curvature points. Line CD is drawn parallel to AB such that the sum of the areas of the parallelogram ACDE and triangle OBE equals the area under the curvature-distance curve, where DE or AC represents the plastic hinge length of the member [1]. Then the elastic and plastic rotation can be defined according to Eqs. (2) and (3), from which θ_p and L_p can be evaluated as shown in Eqs. (4) and (5), respectively. Here, ϕ_y represents the curvature at which, the rebar reaches its yield value, and ϕ_u represents the maximum curvature in the inelastic range.

$$\theta = \int_L \varphi.\mathrm{d}x = \theta_e + \theta_p \tag{1}$$

$$\theta_e = \phi_y \frac{L}{2} \tag{2}$$

$$\theta_p = (\phi_u - \phi_y) L_p \tag{3}$$

$$\theta_p = \theta - \theta_e \tag{4}$$

$$L_p = \frac{\int_L \phi.\mathrm{d}x - \phi_y \frac{L}{2}}{\phi_u - \phi_y}. \tag{5}$$

5.2.2. Experimental method

Beam tip displacement test data from reversed cyclic loading of beam–column joint specimens have been used to determine
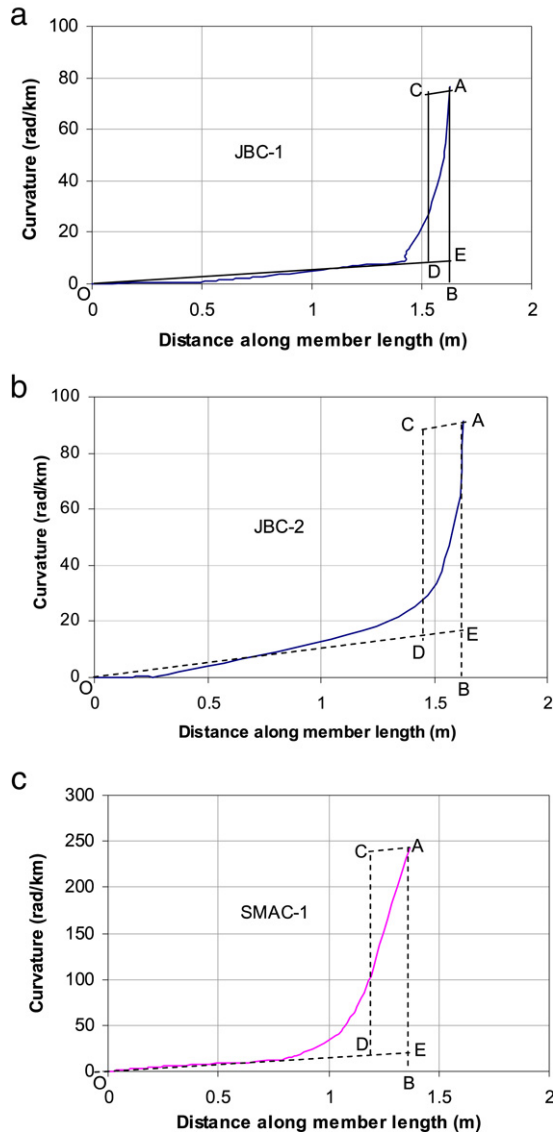
Fig. 6. Curvature distribution along the member length of specimen (a) JBC-1, (b) JBC-2, and (c) SMAC-1.

the real plastic hinge lengths [1]. From force–displacement and moment–curvature test results, bilinear elastic perfectly plastic models have been used to obtain the yield and ultimate values of ϕ_y, ϕ_u, Δ_y and Δ_u. In order to determine the equivalent bilinear curve for the test results, the area under the curve (force–displacement or moment–curvature) is calculated, and then a line having the initial slope of the curve is drawn through the origin. A horizontal line is drawn such that the area under the two lines is equal to the area under the original curve. Then the yield displacement/curvature is defined as the point of intersection between the two lines and the ultimate value is considered as the maximum value of the displacement/curvature in the inelastic range. The Eqs. (6) and (7) can be solved to determine the value of L_p.

$$\Delta_p = \Delta_u - \Delta_y \tag{6}$$

$$\Delta_p = (\phi_u - \phi_y) L_p \left(L - \frac{L_p}{2}\right) \tag{7}$$

where, Δ_y and Δ_u represent the yield and ultimate beam tip displacement from test data, respectively.

5.2.3. Empirical methods

Empirical equations can also be used to estimate L_p for RC members. Numerous models are available. Many of these models consider a proportional increase of L_p with an increase of member length, depth and longitudinal reinforcement dimensions. For instance, models proposed for estimating L_p by Sawyer [30], Corley [31], Mattock [32], and Paulay and Priestley [33] are presented in Eqs. (8)–(11), respectively.

Sawyer [30]: $L_p = 0.075L + 0.25d$ (8)

Corley [31]: $L_p = 0.5d + L/\sqrt{d}$ (9)

Mattock [32]: $L_p = 0.05L + 0.5d_b$ (10)

Paulay and Priestley [33]: $L_p = 0.08L + 0.022d_bf_y$ (11)

where d represents the effective depth of the member in mm, d_b represents the bar diameter in mm, and f_y is the yield strength of the rebar in MPa.

The applicability of these methods for determining L_p of SMA RC members has been investigated and presented in Table 2. The results indicate that the analytical predictions from Eq. (5) provided much lower values compared to those of the experimental results. All the empirical equations underestimated the L_p values for beam–column joints. In the case of SMA-RC column, the estimations from all empirical equations were very close to the experimental value, except for Eq. (8). Eqs. (9) and (10) produced values relatively closer to the experimental results for all three specimens. The best prediction was obtained from Eq. (11), which could estimate the plastic hinge lengths of conventional steel RC members as well as SMA RC members with reasonable accuracy.

5.3. Crack width and crack spacing

Cracking of concrete significantly influences the structural performance of RC members including its stiffness and strength, ductility, energy absorption capacity, corrosion resistance and overall aesthetic appearance. Therefore, it is very important for designers to predict the crack width accurately. This section examines related models available in the literature and compares their results with experimental values for predicting the maximum crack width and average crack spacing of steel RC members and SMA RC members.

Oh and Kang [34] found that steel strain (ε_s), which is directly related to the applied loading, is the most important parameter that affects crack width. Other important variables affecting the crack width include the bar diameter (d_b), concrete clear cover (C), and effective tensile area of concrete (A_{ceff}) based on the energy concept. Oh and Kang [34] proposed the following formulas for predicting the maximum crack width, w_{max} and crack spacing, S_m.

$$w_{max} = a_0 d_b (\varepsilon_s - 0.002) \frac{h_2}{h_1} \tag{12}$$

$$S_m = d_b \left[25.7 \left(\frac{C + d_b/2}{h_2}\right)^{4.5} + 1.66 \left(\frac{A_{ceff}/n}{A_{s1}}\right)^{1/3} + \frac{0.236 \times 10^{-6}}{\varepsilon_s^2} \right] \tag{13}$$

in which, $a_0 = 159 \left(\frac{C+d_b/2}{h_2}\right)^{4.5} + 2.83 \left(\frac{A_{ceff}/n}{A_{s1}}\right)^{1/3}$, $h_1 =$ distance from the centroid of the tension rebar to the neutral axis (mm), $h_2 =$ distance from the extreme tension fiber to the neutral axis (mm), $n =$ number of rebar in the tension zone, and $A_{s1} =$ area of each rebar.

According to CEB-FIP Code [35], the mean crack spacing, S_m is expressed by Eq. (14).

$$S_m = 2\left(C + \frac{S}{10}\right) + K_1 K_2 \frac{d_b}{\rho_{\text{eff}}} \tag{14}$$

where, C = clear concrete cover, S = maximum spacing between longitudinal rebars, d_b = bar diameter, $K_1 = 0.4$ (deformed bar) or 0.8 (plain bar), $K_2 = 0.125(\varepsilon_1 + \varepsilon_2)/\varepsilon_1$ where ε_1 and ε_2 are the maximum and minimum tensile strains in the effective zone, $\rho_{\text{eff}} = A_s/A_{\text{ceff}}$ where A_s = area of rebar in the tensile zone and A_{ceff} = effective tension area of concrete surrounding the tension rebars and having the same centroid as that of the rebars.

The mean (w_m) and maximum crack width ($w_{\max}$) can be calculated using Eqs. (15) and (16), respectively.

$$w_m = \varepsilon_1 S \tag{15}$$
$$w_{\max} = 1.7 w_m. \tag{16}$$

The Canadian Code [27] and the earlier versions of ACI Code [36] adopted Gergely–Lutz equation [37] for predicting crack width of steel RC members (Eq. (17)).

$$w = k f_s \frac{h_2}{h_1} (d_c A)^{1/3}. \tag{17}$$

Here $A = A_{\text{ceff}}/n$, where A_{ceff} is defined earlier for Eq. (13), and n, h_1 and h_2 are defined in Eqs. (12) and (13), d_c = distance from the extreme tension fiber to the center of the rebar located closest to it (mm), f_s = stress in the reinforcement at specified loads calculated using elastic cracked section theory (MPa), and k is a coefficient which is equal to $11 \times 10 - 6$ for conventional RC members, found as $40.9 \times 10^{-6} \pm 9.5 \times 10^{-6}$ for FRP RC members [38].

Chowdhury and Loo [39] predicted the average crack spacing, S_m and the average crack width, w_m and maximum crack width, $w_{\max}$ according to Eqs. (18), (19) and (20), respectively.

$$S_m = 0.6(C - S_{\text{ave}}) + 0.1 d_b/\rho \tag{18}$$
$$w_m = S_m f_s / E_s \tag{19}$$
$$w_{\max} = 1.5 w_m \tag{20}$$

where C and d_b are defined in Eq. (14), S_{ave} = average spacing between rebars, ρ = reinforcement ratio, f_s = stress in rebar at service load, and E_s = modulus of elasticity of rebar.

The Eurocode-2 [40] recommended the following formulas for calculating the average crack spacing, S_m (Eq. (21)) and crack width, w (Eq. (22)) for steel RC members subjected to axial tension and/or bending.

$$S_m = 50 + 0.25 k_1 k_2 d_b/\rho \tag{21}$$
$$w = S_m \cdot \varepsilon_s \cdot \zeta \tag{22}$$

where $k_1 = 1.6$ for plain bars and 0.8 for deformed bars, $k_2 = 0.5$ for members subjected to bending and 1.0 for members subjected to tension, ρ = steel ratio based on the effective concrete area (as defined earlier), d_b = diameter of rebar, ε_s = steel tensile strain, and $\zeta = 1$ for the mean crack width and 1.7 for the maximum crack width.

Table 3 shows the maximum crack width and crack spacing obtained from the above equations for JBC-1 and JBC-2 along with the corresponding experimental results. All the equations, except that of Gergely–Lutz [37] and the Modified Gergely–Lutz equation [38], overestimated the maximum crack width value for steel RC BCJ. Conversely, all the equations underestimated $w_{\max}$ for the SMA RC BCJ. The maximum crack width by the Eurocode-2 [40] was very close to the experimental maximum crack width of JBC-2. It has been observed that in the case of the crack spacing approximation of JBC-1, all the equations could estimate S_m with reasonable accuracy, except Chowdhury and Loo [39]. In the case

of JBC-2, all equations could closely approximate the values for crack spacing, except Oh and Kang [34]. It was also found that the CEB-FIP Code [35] could predict both $w_{\max}$ and S_m for JBC-2 with reasonable accuracy. Overall, the Eurocode-2 [40] was found to be most suitable for estimating both $w_{\max}$ and S_m for steel and SMA RC beam column joints.

5.4. Bond-slip (τ–s) relationship

A moment resisting frame subjected to reversed cyclic loads resulting from a major earthquake is expected to undergo cracks at the column faces. During loading cycles, the longitudinal bars can undergo simultaneous push and pull from opposite sides of the column generating a large demand on anchorage [41] and causing serious bond degradation and slippage of rebars, which in turn will lead to large fixed end rotation between the beams and the columns, along with substantial loss of stiffness and lateral load carrying capacity in subsequent cycles [42]. Although both BCJ specimens were subjected to reversed cyclic loading up to a storey-drift of 8%, the load carrying capacities in both cases increased in subsequent cycles till the end of the test, which implies that the bond degradation and slippage of rebars were not significant for both specimens JBC-1 and JBC-2. Therefore, the bond-slip effect was initially neglected in the subsequent analysis. However, in the case of JBC-2 there may have been some slippage of SMA rebars inside the bar-lock couplers, which resulted in larger rotation at the joint region. The screws of the bar-lock coupler did not penetrate through the SMA bar; they resisted the tensile pull mainly by frictional forces developed at the flat ends of the screws attached on top of the bar, whereas in the case of SMAC-1, the slippage of SMA rebar in the threaded coupler was relatively small compared to that of JBC-2. Therefore, slippage of SMA rebar in SMAC-1 was also neglected in assessing its response. It should be noted that threading large diameter SMA bar is extremely difficult and costly due to its hardness. It may also reduce its strength because of its sensitivity to notches.

5.5. Shear in joint

The joint regions of both specimens JBC-1 and JBC-2 had few diagonal cracks of very fine width and of small length, and remained almost fully intact. The strain measurements on the transverse reinforcement inside the joints of both specimens were similar and much less than their yield strain. This proves that the current design code considers proper detailing of the joint region, thus providing adequate confinement for joint shear resistance.

6. Finite element analysis

In the present section, several inelastic time-history analyses have been performed to predict the performance of steel and SMA RC structural elements using a FE program [23] and compare the results with corresponding experimental data. The FE program is capable of predicting large displacement behaviour of structures taking into account both geometric nonlinearities and material inelasticity. The fibre modelling approach has been employed to represent the distribution of material nonlinearity along the length and cross-sectional area of the member. 3D beam elements have been used for modelling the beam and column where the sectional stress–strain state of the elements is obtained through the integration of the nonlinear uniaxial stress–strain response of the individual fibres in which the section has been subdivided following the spread of material inelasticity within the member cross-section and along the member length. Concrete has been modelled using the nonlinear constant confinement concrete model of Madas [43], which follows the constitutive relationship
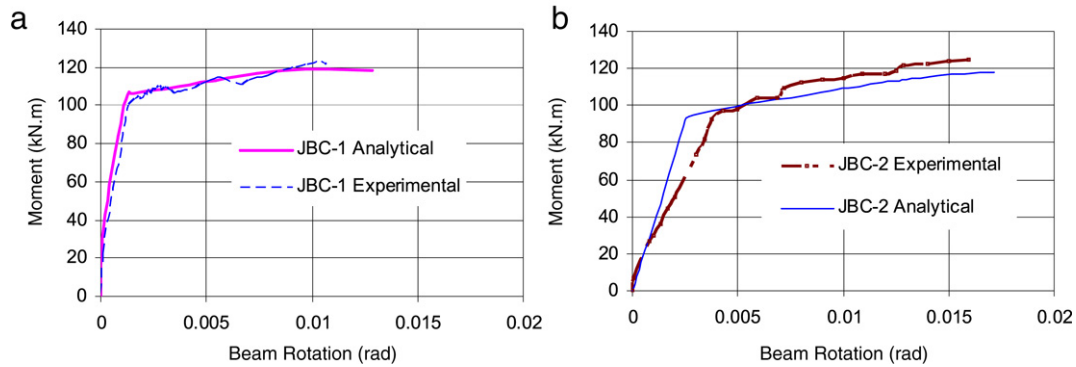
Fig. 7. Comparison between experimental and analytical results of beam moment versus rotation envelope of (a) JBC-1, and (b) JBC-2.

proposed by Mander et al. [44] and the cyclic rules proposed by Martinez-Rueda and Elnashai [45]. The concrete model does not account for tensile softening. Concrete abruptly loses its tensile resistance as soon as the stress reaches its tensile strength. Steel has been modelled using the model of Monti and Nuti [46]. SMA has been modelled according to the model of Auricchio and Sacco [26] as discussed earlier. Fig. 1(b) shows the 1D-superelastic model used in the FE program where SMA has been subjected to multiple stress cycles at a constant temperature and undergoes stress induced transformations. The parameters used to define the material model have already been discussed in Section 3.1 and the values are presented in Table 1. It is to be noted that the SMA model does not account for the gradual increase in residual strain with cycling, which will result in a relatively small amount of residual deformation in the analytical model compared to that of the actual case, i.e. the predicted residual deformations for the SMA RC BCJ are expected to be smaller than those of the observed ones. Since the increase in residual strain is small compared to its recovery strain, disregarding this effect might not be significant for the overall response of the structure.

This section describes FE analyses carried out to validate the results of the FE program with experimental data. The moment–rotation and load–displacement relationship have been used for this purpose.

6.1. Moment versus rotation

A FE mesh has been developed for the beam–column joint specimens JBC-1 and JBC-2 where the geometry and material properties were taken from the experimental data provided by Youssef et al. [15]. The beam and column were divided longitudinally into 15 and 20 elements, respectively. In the case of JBC-2, four of them represent the SMA reinforced part of the beam and the other 11 represent the steel reinforced part. Each element was divided transversely into 200 by 200 fiber elements. Fig. 7(a) and (b) present the predicted results from the FE analysis along with the corresponding experimental results of specimens JBC-1 and JBC-2, respectively showing the envelope of the beam moment–rotation relationship. In all cases, beam rotations were measured at the plastic hinge region of the beam at a distance of 180 mm from the column face. Fig. 7(a) depicts that the FE program could predict the moment–rotation relationship with reasonable accuracy. In the case of JBC-2, the predicted initial stiffness was higher than experimental values. This might be due to slippage of the smooth SMA rebar inside the coupler, which resulted in higher rotation at the joint of the tested specimen. However, the FE program could predict the second branch of the moment–rotation curve and ultimate moment carrying capacity accurately. The predicted moment and its corresponding rotation at the last cycle of loading were 118 kN and 0.0172 rad respectively, which were only 5.4% smaller and 7.5% higher than the corresponding experimental values.

6.2. Load–displacement relationship

This section describes the load–displacement relationship obtained from the FE analysis in order to validate the results of the FE programme.

6.2.1. Steel RC BCJ

Fig. 8(a) illustrates the beam tip load versus beam tip displacement for the steel RC BCJ, while Fig. 8(b) shows the corresponding results predicted by the FE analysis. The ultimate beam tip load was predicted as 64.5 kN at a tip displacement of 72 mm compared to the experimental result of 65.5 kN at the same tip displacement. The predicted maximum residual beam tip displacement was found as 44 mm, whereas the experimental value was 45 mm. The total predicted energy dissipation was 30.5 kN m, which is 15% higher than the corresponding experimental value (Fig. 9(a)). The numerical results show that the FE program is capable of predicting the force–displacement behaviour of the joint with reasonable accuracy.

6.2.2. SMA RC BCJ

Fig. 8(c) presents the experimental results of the specimen tested, showing the beam tip load versus beam tip displacement. Fig. 8(d) illustrates the numerical results predicted by the FE analysis. The ultimate beam tip load was predicted as 62.7 kN at a tip displacement of 72 mm compared to the experimental result of 68.1 kN at the same tip displacement. The total predicted energy dissipation was 19.7 kN m, which is 17% higher than that of the experimental value. Besides the variation in initial stiffness of the predicted load–displacement relationship compared to that of the experimental results, the numerical model was capable of predicting the force–displacement behaviour of the SMA RC joint with reasonable accuracy. The disparity in the initial stiffness might be due to slippage of the smooth SMA rebars in the joint region of the tested specimen. The predicted results using the FE technique can be refined by introducing proper bond-slip model at the joint region as described earlier. The bond-slip relationship can also be incorporated at the joint region of the FE model by applying a rotational spring simulating the slippage of SMA rebar.

An experimental investigation was carried out to determine the slippage of SMA rebars through couplers by a simple pullout test. Steel and SMA rebars were inserted at each end of the coupler, the screw heads were sheared off by applying prescribed torques. Then the coupler arrangement was tested using a universal testing machine under tension only. An extensometer was clamped to the steel and SMA rebars to determine the change in length. The slippage, s inside the coupler was then calculated by subtracting the axial elongation of steel (s_{st}) and SMA (s_{SMA}) rebars due to tensile forces from the extensiometer reading, s_e (Eq. (21)). Fig. 10 illustrates the bar force versus slippage of SMA rebar in the coupler.
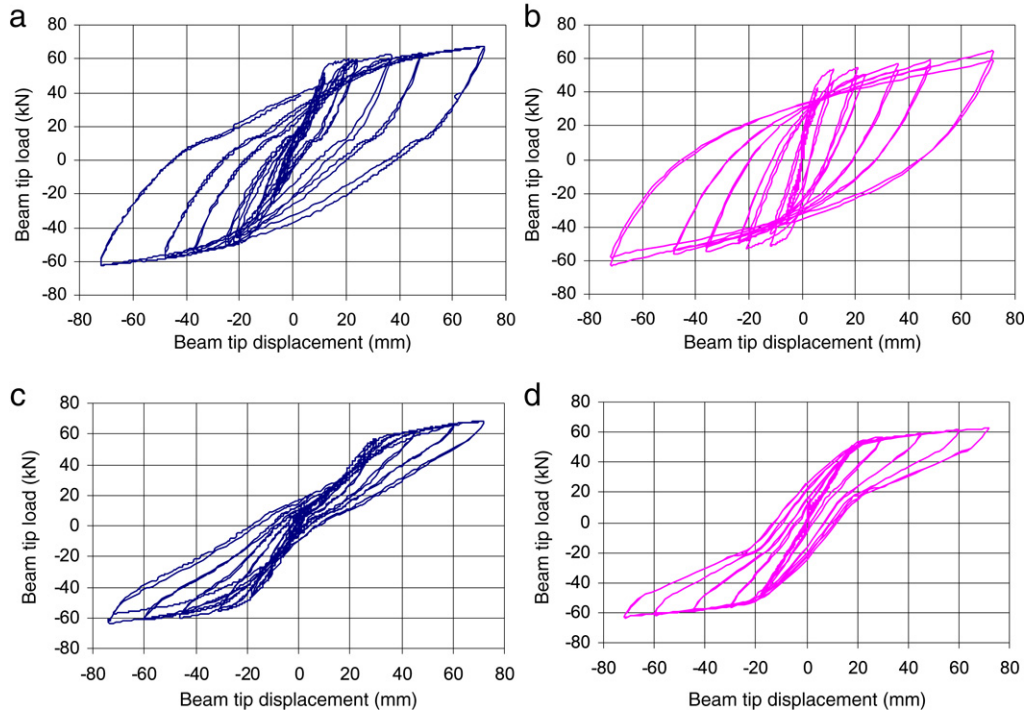
Fig. 8. Beam tip-load versus tip-displacement: (a) experimental result of JBC-1, (b) analytical result of JBC-1, (c) experimental result of JBC-2, and (d) analytical result of JBC-2 (without bond-slip).
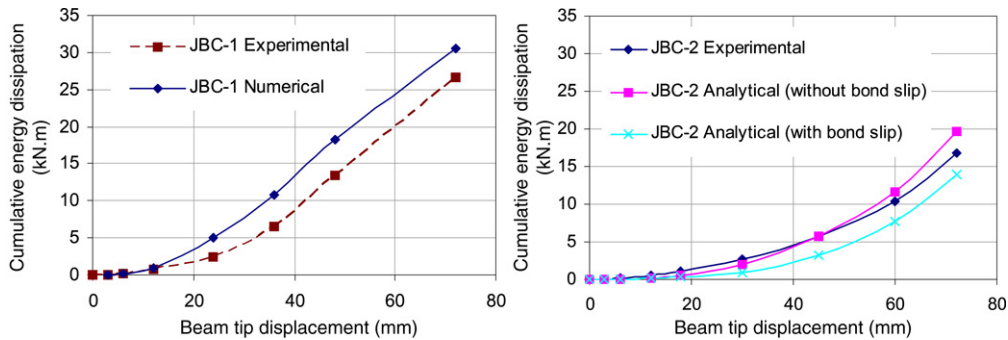

Fig. 9. Cumulative energy dissipation showing both experimental and analytical results by specimens (a) JBC-1 and (b) JBC-2.
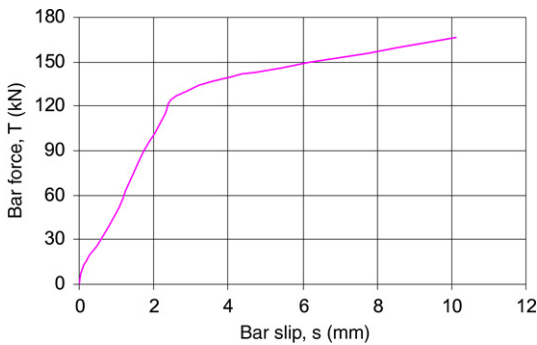

Fig. 10. Resultant bar slip, s inside the coupler with respect to bar force, T.

This figure was then used to construct the moment–rotation relationship. From numerical analysis, the bar force, T is calculated for a corresponding beam tip load, P (Fig. 11(a)). Using the relationship of Fig. 10 the slip at the joint, s is obtained, which allows calculating beam rotation, θ (Eq. (22)) due to bar slip.

$$s = s_e - s_{st} - s_{SMA} \tag{23}$$

$$\theta = s/(h - d') \tag{24}$$

where, h is the beam depth and d' is the distance from the centre of the top bar to the top beam face. After calculating θ, the corresponding moment is calculated by multiplying the moment arm with P. Repeating the same procedure, the moment–rotation relationship is established as shown in Fig. 11(b). This relationship has been used for the analytical model of JBC-2, which has been represented by a rotational spring at its joint. The adapted FE model is presented in Fig. 12(a). The numerical results predicted by the new model show good agreement with the experimental results varying by 11% for beam tip load under an equal amount of tip displacement as shown in Fig. 13. The predicted initial stiffness was similar to the experimental result. The cumulative energy dissipation was found to be 16.7 kN m from the load–displacement curve of the test result, whereas the amount of energy dissipation obtained from the predicted result was 14.0 kN m, which is 16.2% lower than the experimental result (Fig. 9(b)). The use of smooth SMA rebars resulted in the formation of a large crack at a distance of approximately half of the beam-depth away from the column face. However, this slippage also reduced the energy dissipation capacity of JBC-2.
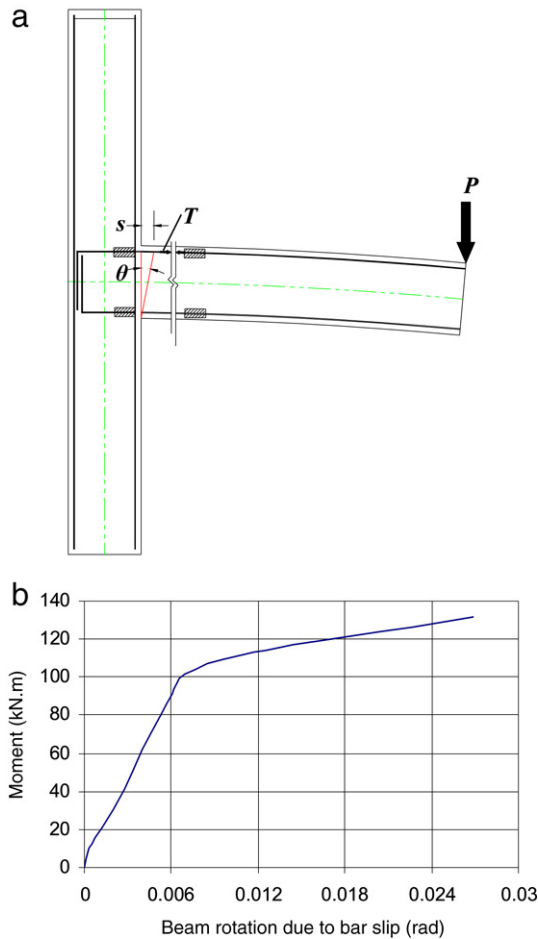
a

b

Fig. 11. (a) SMA bar slips at the joint due to beam-tip load, (b) moment–rotation relationship due to bar slip.

6.2.3. SMA RC column

Two quarter-scale spiral RC columns representing RC bridge piers were designed, constructed and tested using a shake table by Saiidi and Wang [14]. SMA rebars were placed at the plastic hinge region and connected to the steel rebars with mechanical threaded couplers. Fig. 15(a) shows the performance of the bridge pier under shake table testing. An inelastic dynamic analysis has been performed to predict the performance of the bridge pier tested by Saiidi and Wang [14]. SMA has been modelled according to Figs. 1(b) and 2. A finite element model for the bridge pier is
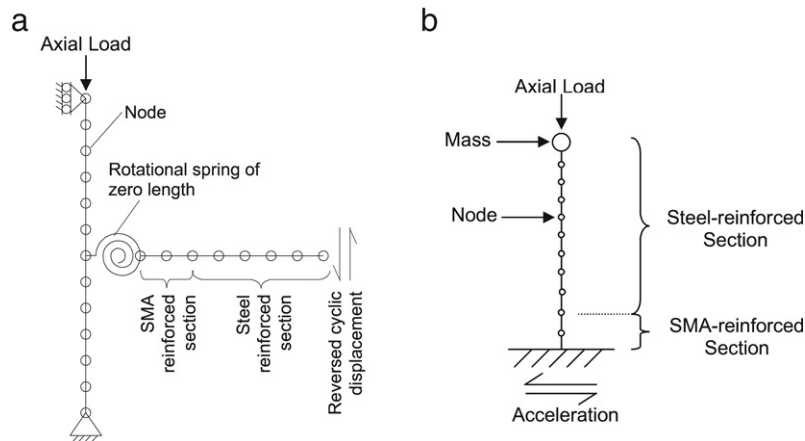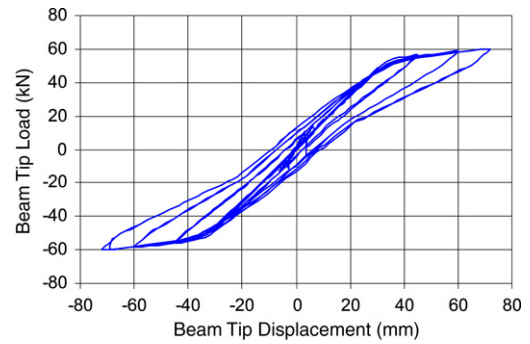

Fig. 13. Beam tip load–displacement relationships of specimen JBC-2 from analytical results with bond-slip model.
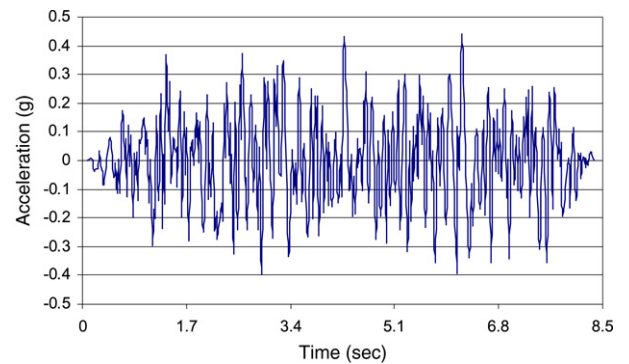

Fig. 14. Base acceleration time-history applied in SMA-reinforced concrete column (Saiidi and Wang [14], with permission).

shown in Fig. 12(b). Here no special modelling technique has been incorporated for bar couplers since experimental results showed full capacity for transferring forces from SMA to steel rebar with negligible slippage. The pier was subjected to a series of scaled motions ranging from 15% to 300% of the base acceleration time history as shown in Fig. 14. Fig. 15(b) depicts the predicted base shear-tip displacement of the numerical model which seems to be fairly accurate as compared to the experimental results of Saiidi and Wang [14] shown in Fig. 15(a). The maximum base shear and the tip displacement were predicted as 81.5 kN and 62.0 mm compared to experimental values of 77.2 kN and 66.0 mm, respectively. The numerical results predicted by the FE model show good agreement with corresponding experimental results varying only by 5.6% for the base shear and 6.1% for the tip displacement. The cumulative energy dissipation was calculated as 48.2 kN m from the predicted load–displacement curve, whereas the amount
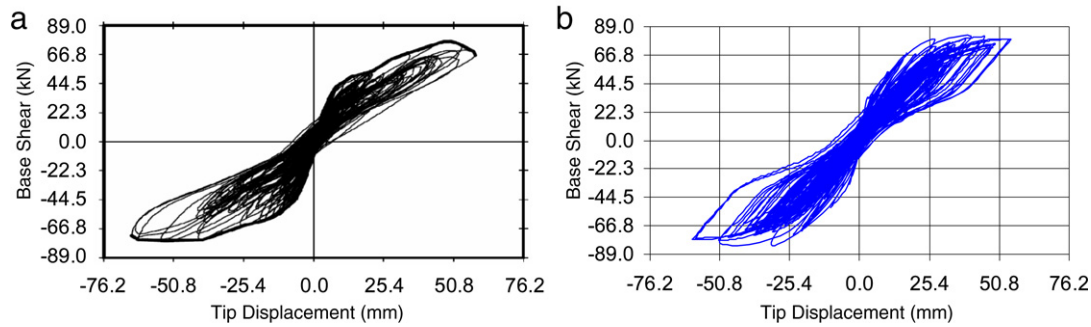
a

b

Fig. 12. (a) FE model of a SMA-RC exterior joint, where bond-slip is incorporated by a rotational spring, (b) FE model of SMA-RC column.

Fig. 15. Base shear versus tip-displacement for SMA-RC bridge pier: (a) experimental results (Saiidi and Wang [14], with permission), and (b) analytical results.

of energy dissipation obtained from the experimental result was 44.0 kN m, which is only 9.4% lower than the calculated result. The SMA-RC column failed by concrete crushing and yielding of SMA rebar within the superelastic strain range and the displacement ductility was measured as 5.9, whereas in the numerical analysis, the model also failed due to crushing of concrete and yielding of SMA within superelastic strain limit with a displacement ductility of 6.7.

7. Discussion

The hysteretic load–displacement curves of JBC-2 and SMAC-1 exhibited better performance compared with that of JBC-1 in terms of residual displacements remaining in the joint after unloading. The flag-shaped stress–strain hysteresis of superelastic SMA bars produced flag-shaped hysteretic load–displacement curves in the SMA-RC beam–column elements (JBC-2 and SMAC-1). Although the steel-RC beam–column joint (JBC-1) dissipated a relatively higher amount of energy compared to that of JBC-2 because of its large hysteretic loops, JBC-2 performed better because of its capability in recovering post-elastic strain, which makes it very attractive in highly seismic regions where the beam–column joints can dissipate significant amounts of energy and remain functional even after a strong earthquake.

Excessive lateral displacement and residual displacement have been identified as the major causes of failure of buildings and bridges during earthquakes. SMAs are unique materials that can recover strains almost fully even after large inelastic deformations. If SMA can be used as reinforcement in beam–column elements, it can initiate major progress in seismic design whereby the repair cost can be substantially reduced and the structure may remain serviceable even after a severe earthquake. The developed numerical model can be used to simulate the behaviour of superelastic SMA-RC multi-storey concrete frames with high degrees of redundancy, and accordingly predict the progress of failure and its performance under earthquake loading. The numerical results can also be used for performance-based design guidelines. Devoted research effort is still required to address many issues and uncertainties before the widespread use of SMA as concrete reinforcement to make it safe and competitive in seismic areas for large-scale structural applications.

8. Conclusions

This paper discusses a novel approach to reduce the seismic vulnerability of RC structures by utilizing smart materials such as SMA in beam–column elements. The objective of this study is to make analytical prediction of the behavior of steel and SMA-RC beam–column joints in terms of crack width and crack spacing, plastic hinge length, moment–rotation and load–displacement relationship and compare them with the corresponding experimental results. Based on this work, the following conclusions can be drawn.

- An incremental deformation technique can be used to determine the moment and its corresponding curvature at a particular strain distribution both for steel and SMA-RC members.
- The plastic hinge lengths for steel and SMA RC beam–column joints have been determined with a number of methods. The Paulay and Priestley equation [33] has been found to be most suitable for both cases.
- For predicting the average crack spacing and maximum crack width, Eurocode-2 [40] has been found fairly accurate for both steel and SMA RC beam–column joints.
- Both specimens JBC-1 and JBC-2 have been analyzed under cyclic displacement loading with the use of a FE program and their performances have been compared with corresponding experimental results. The FE program has also been validated using experimental results for a column-foundation joint reinforced with SMA-steel coupled reinforcement at its plastic hinge location. Numerical results indicate that the FE program can predict the moment–rotation and load–displacement curve with reasonable accuracy.
- An adequate bond-slip model should be incorporated for an accurate prediction of the load–displacement relationship while using barlock type couplers.

References

[1] Park R, Paulay T. Reinforced concrete structures. New York: John Wiley & Sons Inc; 1975. 769 pages.
[2] Alam MS, Youssef MA, Nehdi M. Utilizing shape memory alloys to enhance the performance and safety of civil infrastructure: A review. Canadian J Civil Eng 2007;34:1075–86.
[3] Tamai H, Miura K, Kitagawa Y, Fukuta T. Application of SMA rod to exposed-type column base in smart structural system. The Proc. SPIE 2003;5057: 169–77.
[4] Dolce M, Cardone D, Marnetto R, Mucciarelli M, Nigro D, Ponzo FC. et al. Experimental static and dynamic response of a real RC frame upgraded with SMA re-centering and dissipating braces. In: The proc. of the 13th world conf. on earthquake engg. 2004; Paper no. 2878.
[5] Maji AK, Negret I. Smart prestressing with shape memory alloy. J Eng Mech 1998;124(10):1121–8.
[6] Clark PW, Aiken ID, Kelly JM, Higashino M, Krumme R. Experimental and analytical studies of shape-memory alloy dampers for structural control. The Proc. of SPIE 1995;2445:241–51.
[7] Dolce M, Cardone D, Ponzo FC. Shaking-table tests on reinforced concrete frames with different isolation systems. Earthquake Eng Struct Dynam 2007; 36:573–96.
[8] Andrawes B, Desroches R. Unseating prevention for multiple frame bridges using superelastic devices. Smart Mater Struct 2005;14(3): S60–7.
[9] Ocel J, DesRoches R, Leon RT, Krumme R, Hayes JR, Sweeny S. Steel beam–column connections using shape memory alloys. J Struct Eng, ASCE 2004;130:732–40.
[10] Auricchio F, Fugazza D, DesRoches R. Earthquake performance of steel frames with Nitinol braces. J Earthquake Eng 2006;10(SPEC):45–66.
[11] Zhu S, Zhang Y. Seismic behaviour of self-centring braced frame buildings with reusable hysteretic damping brace. Earthquake Engineering and Structural Dynamics 2007;36:1329–46.
[12] Krstulovic-Opara N, Nau J, Wriggers P, Krstulovic-Opara L. Self-actuating SMA-HPFRC fuses for auto-adaptive composite structures. Comput Aided Civil Infrastructure Eng 2003;18:78–94.

[13] Saiidi MS, Zadeh MS, Ayoub C, Itani A. Pilot study of behavior of concrete beams reinforced with shape memory alloys. J Mater Civil Eng, ASCE 2007; 19(6):454–61.

[14] Saiidi MS, Wang H. Exploratory study of seismic response of concrete columns with shape memory alloys reinforcement. ACI Struct J 2006;103:435–42.

[15] Youssef MA, Alam MS, Nehdi M. Experimental investigation on the seismic behaviour of beam–column joints reinforced with superelastic shape memory alloys. J Earthquake Eng 2008 [in press].

[16] Wilson JC, Wesolowsky MJ. Shape memory alloys for seismic response modification: A state-of-the-art review. Earthquake Spectra 2005;21(2): 569–601.

[17] Tanaka K, Nagaki S. Thermomechanical desription of materials with internal variables in the process of phase transitions. Ingenieur-Archiv 1982;51(5): 287–99.

[18] Liang C, Rogers CA. One-dimensional thermomechanical constitutive relations for shape memory materials. Collection of Technical Papers — AIAA/ASME/ASCE/AHS structures, structural dynamics & materials conference, n pt 1. 1990. p. 16–28.

[19] Brinson LC. One-dimensional constitutive behavior of shape memory alloys: Thermomechanical derivation with non-constant material functions and redefined martensite internal variable. J Intelligent Materl Syst Struct 1993; 4(2):229–42.

[20] Auricchio F, Lubliner J. Uniaxial model for shape-memory alloys. Internat J Solids Struct 1997;34(27):3601–18.

[21] ANSYS, Inc. Version 10.0. South Pointe, Canonsburg, PA (USA); 2005.

[22] Hibbitt, Karlsson, Sorensen. Abaqus user's manual, Version 6.4, Pawtucket (RI); 2003.

[23] SeismoStruct Help file 2007, Version 4.0.2. Accessed on Feb 2007. Available at: http://www.seismosoft.com/SeismoStruct/index.htm.

[24] Auricchio F, Taylor RL, Lubliner J. Shape-memory alloys: Macromodelling and numerical simulations of the superelastic behaviour. Comput Methods Appl Mech Eng 1997;146(3–4):281–312.

[25] Auricchio F, Taylor RL. Shape memory alloy superelastic behavior: 3D finite-element simulations. The Proc. of SPIE 1996;2779:487–92.

[26] Auricchio F, Sacco E. Superelastic shape-memory-alloy beam model. J Intelligent Materl Syst Struct 1997;8(6):489–501.

[27] Design of Concrete Structures. CSA A23.3-04, Canadian Standards Association, Rexdale, Ontario (Canada); 2004, 240 pages.

[28] Barsplice Products Inc. Zap Screwlok® Mechanical splices and connectors for reinforcing bars—review, visited on April 08, 2006. Available at: http://www.barsplice.com/BPI_Scans/Zap_Data-Sheet_RevA.pdf.

[29] Scott BD, Park R, Priestley MJN. Stress–strain behavior of concrete confined by overlapping hoops at low and high strain rates. ACI Struct J 1982;79(1):13–27.

[30] Sawyer HA. Design of concrete frames for two failure stages. In: Proceedings international symposium on the flexural mechanics of reinforced concrete; Miami 1964; ACI SP-12:405-431.

[31] Corley WG. Rotational capacity of reinforced concrete beams. J Struct Division, ASCE 1966;92(ST5):121–6.

[32] Mattock AH. Discussion of 'Rotational capacity of reinforced concrete beams', by WG Corley. J Struct Division, ASCE 1967;93(2):519–22.

[33] Paulay T, Priestley MJN. Seismic design of reinforced concrete and masonry buildings. New York: John Wiley & Sons, Inc.; 1992.

[34] Oh BH, Kang YJ. New formulas for maximum crack width and crack spacing in reinforced concrete flexural members. ACI Struct J 1987;84:103–12.

[35] CEB-FIP. Model code for concrete structures. Comite Euro-International du Beton, Thomas Telford: London (UK); 1990.

[36] ACI Committee 318. Building code requirements for structural concrete and commentary. Farmington Hills (MI): American Concrete Institute; 1995.

[37] Gergely P, Lutz LA. Maximum crack width in reinforced concrete flexural members. In: Causes mechanism and control of cracking in concrete, ACI Publication. Detriot: American Concrete Institute; 1973. SP-20: 87–117.

[38] Masmoudi R, Thériault M, Benmokrane B. Flexural behavior of concrete beams reinforced with deformed fiber reinforced plastic reinforcing rods. ACI Struct J 1998;95:665–76.

[39] Chowdhury SH, Loo YC. Crack width formula for reinforced and partially prestressed concrete beams. In: Dayaratnam P, Ramana Rao NV, editors. Proceedings, international conference on maintenance and durability of concrete structures 1997. Hyderabad (India): JNT University. p. 46–51.

[40] ENV 1992-1-1, Eurocode 2. Design of concrete structures—Part 1: General rules and rules for buildings. 1991.

[41] Viwathanatepa S, Popov EP, Bertero VV. Effects of generalized loadings on bond of reinforcing bars embedded in concrete blocks. Report no. UCB/EERC-79/22. Berkeley (California); 1979.

[42] Filippou FC, Popov EP, Bertero VV. Effects of bond deterioration on hysteretic behavior of reinforced concrete joints. Report no. UCB/EERC-83/19. Berkeley: University of California; 1983.

[43] Madas P. Advanced modelling of composite frames subjected to earthquake loading, Ph.D. thesis. London (UK): Imperial College, University of London; 1993.

[44] Mander JB, Priestley MJN, Park R. Theoretical stress–strain model for confined concrete. J Struct Eng, ASCE 1998;114(8):1804–26.

[45] Martinez-Rueda JE, Elnashai AS. Confined concrete model under cyclic load. Mater Struct 1997;30(3):139–47.

[46] Monti G, Nuti C. Nonlinear cyclic behaviour of reinforcing bars including buckling. J Struct Eng, ASCE 1992;118(12):3268–84.